Toward Real-World Super-Resolution via Adaptive Downsampling Models

Sanghyun Son*, Jaeha Kim*, Wei-Sheng Lai, Ming-Hsuan Yang, and Kyoung Mu Lee *Fellow, IEEE,*

APPENDIX A
DETAILS ABOUT THE LOW-PASS FILTERS

Formulation of the low-pass filters. We describe specific implementations of low-pass filters in the proposed LFL formulation. Our LFL utilizes conventional low-pass filters to extract low-frequency components from given images. Therefore, we replace the term LPF_* in (4) to a kernel representation k_{HR} and k_{Down} to simplify the description as follows:

$$\mathcal{L}_{\text{LFL}} = \left\| \left(\mathbf{I}_{\text{HR}} * k_{\text{HR}}\right)_{\downarrow ms} - \left(\mathbf{I}_{\text{Down}} * k_{\text{Down}}\right)_{\downarrow m} \right\|_1, \tag{A}$$

where m is a subsampling factor of the LR image, and (A) is equivalent to (4) in our main manuscript. For example, our default LFL_m formulation corresponds to a 2D kernel k_{Down} of $m \times m$ where $k_{\text{Down}}(x, y) \equiv 1/m^2$. We note that $m = 16$ is used throughout our studies. In $\times 2$ downsamping case, a kernel k_{HR} for HR images can be expressed as a box filter of 32×32 with $k_{\text{HR}}(x, y) \equiv 1/32^2$. Here, (x, y) describes a coordinate system of the downsampling kernel, including a sub-pixel shift. Specifically, a center of the 16×16 kernel, which is not a pixel, corresponds to $k(0, 0)$ and neighboring 4 pixels are represented as $k(\pm 0.5, \pm 0.5)$, respectively. This formulation is useful for Gaussian kernels on an even-sized grid as follows:

$$k(x, y) = \frac{1}{Z} \exp\left(-\frac{x^2}{2\sigma_x^2} - \frac{y^2}{2\sigma_y^2}\right), \tag{B}$$

where Z is a normalization factor so that $\sum_{x,y} k(x, y) \equiv 1$. For the proposed LFL, only isotropic cases are tested where σ_x and σ_y are equal. In the Gaussian cases, we follow a convention and set the kernel grid size to $p \times p$ where p is the nearest power of two from $6\sigma_x$. While we adopt the filtering-based method for our LFL for simplicity, more complex formulations such as Wavelet can be introduced without losing generality.

Selection of the low-pass filters. An appropriate selection of the low-pass filter in our LFL plays an essential role.

TABLE A
Specifications of low-pass filters we use.
For box and Gaussian filters, weights are normalized so that their values are summed to 1. We note that a subsampling by ms and m follow after LPF_{ms} and LPF_s, respectively, to reduce image resolutions. More details about the filters are described in Appendix A.

Type	Filter	Size	Shape
2D Box	LPF_{ms} LPF_s	$ms \times ms$ $m \times m$	$ms \times ms$ box $m \times m$ box
2D Gaussian	LPF_{ms} LPF_s	$ms \times ms$ $m \times m$	$\sigma_x = \sigma_y = s\sigma$ $\sigma_x = \sigma_y = \sigma$

TABLE B
Ablation study on the shapes and sizes of LPF_m.
We train the LFL-based downsampler and the following SR model on DIV2K $\times 2$ (k_4) to observe how different low-pass filters affect the performance of our approach.

(a) Box filters for LPF_m

Method \ Box size m	PSNR↑(dB) for $\times 2$ SR (k_4) 2	4	8	16	32	64
LFL + EDSR (**Proposed**)	29.51	30.17	31.06	31.57	**31.58**	28.11

(b) Gaussian filters for LPF_m

Method \ Gaussian sigma σ	PSNR↑ for $\times 2$ SR (k_4) 0.8	1.2	1.6	2.0	2.5	3.0
LFL + EDSR (**Proposed**)	29.64	30.24	30.42	30.62	30.96	30.75

Therefore, we conduct an extensive ablation study to determine the low-pass filter when training the downsampler $\mathcal{D}$. Table B shows how different types and shapes of low-pass filters for the downsampler affect the SR results. We present the performance evaluation on the synthetic DIV2K dataset with a challenging anisotropic Gaussian kernel k_4. As shown in Table 2(a), a small box filter, e.g., $m = 2$, may bias the training objective and degrade the following SR performance. On the other hand, a large box filter with $m = 64$ operates as an extremely loose constraint and cannot contribute to preserving image contents across different scales. In Table 2(b), we have also introduced 2D Gaussian filters for the LFL. However, simple box filters have demonstrated relatively better performance. Thus, we use 16×16 box filters for the low-pass filter LPF_m and 32×32 for LPF_{ms} by default throughout our experiments.

- *Authors contributed equally.
- S. Son, J. Kim, and K. M. Lee are with the Department of ECE & ASRI, Seoul National University, Seoul, Korea, 08826. E-mail: {thstkdgus35, hyjkim2, kyoungmu}@snu.ac.kr
- W.-S. Lai and Ming-Hsuan are with Google Research. E-mail: {wslai, minghsuan}@google.com

TABLE C
Detailed parameters to implement the synthetic Gaussian kernels. Fig. 5 in our main manuscript also visualizes each downsampling kernel in detail.

Kernel k_i	σ_x	σ_y	θ	Type
k_1	1.0	1.0	0°	Isotropic
k_2	1.6	1.6	0°	Isotropic
k_3	1.0	2.0	0°	Anisotropic
k_4	1.0	2.0	29°	Anisotropic

APPENDIX B
DETAILS ABOUT THE SYNTHETIC KERNELS

We present a formulation of the $\times 2$ synthetic downsampling kernels used for various experiments in our main manuscript. As we describe in Section 4.1, k_0 denotes a widely-used MATLAB bicubic kernel. The other kernels, i.e., $k_1 \sim k_4$, are 20×20 and sampled from a standard 2D Gaussian distribution following (B). Table C describes the actual parameters used to instantiate our synthetic kernels. To validate the generalization ability of the proposed method, we do not resort to radial kernels that are relatively easy to model and introduce anisotropic kernels k_3 and k_4. The most challenging case k_4 further includes rotation of random degrees θ and have neither vertical nor horizontal symmetries. For a larger $\times 4$ downsampling factor, we follow an approach from KernelGAN [2] and convolve the same kernel twice to generate a larger one.

APPENDIX C
STABILITY OF THE PROPOSED METHODS

Since our LFL and ADL rely on unsupervised adversarial training, stability and reproducibility of the proposed method can be an essential issue. Therefore, we conduct five independent experiments for each of the five downsampling kernels $k_0 \sim k_4$ at a scale factor of $\times 2$ t analyze the stability of our training scheme. Fig. A shows the average performance of the following SR model after we train the downsampler using LFL and ADL, across five different kernel configurations on the synthetic DIV2K dataset. Even in the unsupervised learning framework, the SR model with our LFL and ADL schemes performs consistently with a small variation. Since the SR model performs stably across different experimental configurations, we report the result from one single run in the other sections.

APPENDIX D
DETAILED COMPARISON WITH KERNELGAN

Table 4 in our main manuscript shows that the proposed ADL + EDSR outperforms the KernelGAN + ZSSR combination by a significant margin even when only one LR image is available for the training. In this section, we use multiple images to train KernelGAN to demonstrate the advantage of our method when large-scale unpaired images are available. Table D shows extensive experimental results regarding different training datasets of the KernelGAN. We note that ZSSR is used to reconstruct $\mathbf{I}_{\text{SR}}$ following KernelGAN by default unless mentioned otherwise.

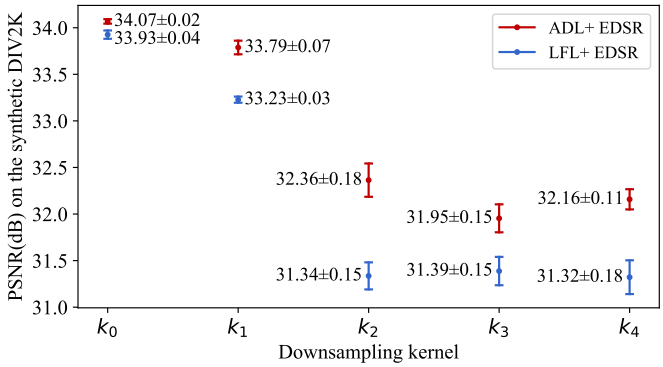

Fig. A. **Stability analysis of the proposed methods.** We visualize the average performance of the baseline EDSR $\times 2$ model and standard deviation from five runs on each downsampling kernel. Notably, ADL consistently outperforms LFL in all synthetic downsampling kernel configurations.

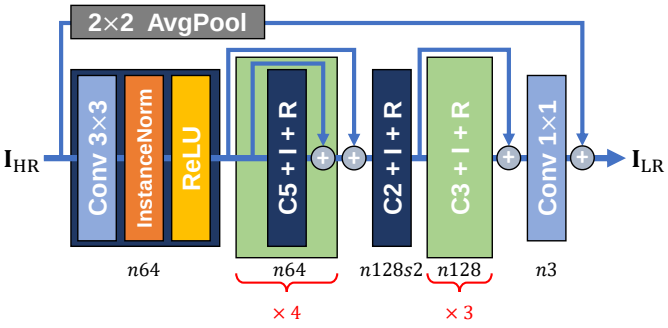

(a) Downsampling CNN $\mathcal{D}$

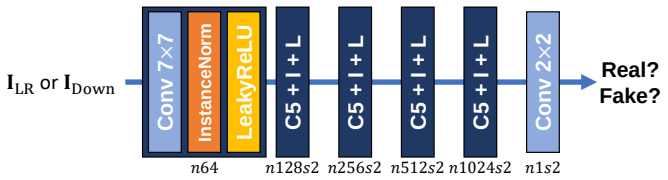

(b) Discriminator CNN $\mathcal{F}$

Fig. B. **Our CNN architectures.** CK in the **navy** box denotes a $K \times K$ convolutional layer, e.g., C5 for 5×5. For a sequence of the convolutional, instance normalization [14], and ReLU (or LeakyReLU [12]) activation layers, we use the term CK + I + R (or L) for simplicity. The green block in (a) incorporates a shortcut connection wrapping around the CK + I + R sequence. We note that n refers to the number of output channels, and s describes the stride of the convolutional layer with a default value of 1, respectively.

First, in Cases 1 and 2, we modify KernelGAN to use 100 validation LR images as a training dataset and predict a shared downsampling kernel rather than calculate it for each image. This configuration demonstrates how KernelGAN operates on large-scale data. Using the estimated kernel, ZSSR is applied to each image independently. Compared to the original KernelGAN + ZSSR configuration, i.e., Case 0, using more images for kernel estimation has demonstrated inconsistent performance variations on synthetic kernel experiments $k_0 \sim k_4$ in Case 1. For the kernels k_2 and k_3, using more data has brought noticeable performance improvements. However, with the kernels k_0, k_1, and k_4, using a single image yields better results.

The capacity of ZSSR is relatively smaller than recent state-of-the-art methods, which may limit the performance

TABLE D
Ablation study on using more data for the KernelGAN method.
HR images correspond to inputs of the $\mathbf{I}_{\text{LR}}$ generator, i.e., the deep linear generator for KernelGAN experiments and our downsampling network for the ADL configuration, while LR images are *real* samples for the discriminator network. We note that Case 0 and ADL correspond to Table 4 in our main manuscript. EDSR denotes a baseline version that has 1.4M parameters. All evaluations are done using DIV2K '*0801.png*'∼'*0900.png*.'

Case	Dataset for the $\mathbf{I}_{\text{LR}}$ Generator HR image(s)	LR image(s)	SR model	PSNR$^{\uparrow}$(dB) for $\times 2$ SR k_0	k_1	k_2	k_3	k_4
1	'*0801*'∼'*0900*'		ZSSR	21.54	26.41	30.55	31.18	27.68
2			EDSR	16.87	18.55	29.95	31.08	23.28
3	'*0001*'∼'*0400*'	'*0401*'∼'*0800*'	ZSSR	20.91	26.83	29.97	28.46	27.99
4			EDSR	16.11	20.35	29.26	24.85	19.68
0	$\mathbf{I}_{\text{LR}}$	$\mathbf{I}_{\text{LR}}$	ZSSR	22.32	26.42	30.44	29.10	29.12
ADL	'*0001*'∼'*0400*'	'*0401*'∼'*0800*'	EDSR	**34.07**	**33.68**	**32.51**	**32.08**	**32.05**

of the KernelGAN + ZSSR combination. Specifically, the model has only 0.2M parameters and uses a single image for training. Therefore, we introduce a larger EDSR-baseline model as an SR backbone network with 400 training samples in Case 2. Similar to the proposed LFL and ADL experiments in our main manuscript, we synthesize 400 LR images from DIV2K '*0001.png*'∼'*0400.png*' using the estimated kernel from the KernelGAN model. The following EDSR is then trained on the synthetic LR-HR pairs. However, the final SR performance decreases, while EDSR-baseline has a larger capacity than ZSSR. Unlike our ADL which brings additional performance gains with a larger SR backbone (see ADL + EDSR and ADL + RRDB in Table 4), such behavior demonstrates that better fitting to the kernel from KernelGAN does not guarantee higher SR performance.

In Cases 3 and 4, we adopt the same dataset configuration as the proposed LFL and ADL, i.e., 400 HR images with unpaired 400 LR samples, when training KernelGAN. Therefore, the only difference between our and KernelGAN algorithms is model architectures (nonlinear CNN vs. deep linear generator) and loss functions (adaptive downsampling loss vs. kernel constraints). We first estimate the shared kernel k by feeding $\mathbf{I}_{\text{HR}}$ to the deep linear generator, and the discriminator is optimized to distinguish the output of the downsampling model and real LR images $\mathbf{I}_{\text{LR}}$ synthesized by a ground-truth kernel k_i. In Case 3, ZSSR is applied to '*0801.png*'∼'*0900.png*' independently using a single shared kernel. In Case 4, we train EDSR similar to Case 2. We note that the only difference between Cases 1, 2, and Cases 3, 4 is a training dataset for the generator, i.e., downsampling model in KernelGAN.

To summarize, our ADL + EDSR or ADL + RRDB formulation show consistently better performance compared to KernelGAN regardless of the number of training data and model capacity.

APPENDIX E
NETWORK ARCHITECTURE

Fig. B illustrates CNN architectures we use throughout our main manuscript. The downsampling network adopts the residual connections [6] and instance normalization [14] strategy for easier optimization. A global residual connection [9] with 2×2 average pooling operation is also introduced to provide a stable starting point. We note that the 2×2 average pooling in Figure B(a) *does not* operate as a restrictive prior which instabilizes the adversarial training objective, since it does not force the output $\mathbf{I}_{\text{Down}}$ to be a specific function of the input $\mathbf{I}_{\text{HR}}$. Unlike the KernelGAN [2] model, our downsampling CNN incorporates nonlinear ReLU activations and thus can learn a more generalized function. Our discriminator network is fully convolutional [8] and returns a 2×2 probability map from a 64×64 input patch. Both of the downsampling and discriminator CNNs are initialized with weights of random Gaussian $\mathcal{N}\left(0, 0.02^2\right)$.

APPENDIX F
DETAILS ABOUT THE HYPERPARAMETERS

We present detailed hyperparameters and experimental configurations that are not described in our main manuscript. In the downsampling task, i.e., Algorithm 1 and (2) in our main manuscript, we set the learning rate of η of downsampling and discriminator CNNs $\mathcal{D}$ and $\mathcal{F}$ to 5×10^{-5}. For each iteration, we use 32 samples of patch size 128×128 as an input batch and generate LR images of 64×64. To train SR models, we use a batch size of 16 with 48×48 input images. The learning rate is set to 10^{-4}, similar to conventional approaches for deep image super-resolution [5], [11], [16]. The only differences are that we reduce the learning rate by half for every 50 epochs and our baseline EDSR [11] model is trained for 200 epochs, not 300, as validation performance does not change after then. In all experiments, pixel values are normalized from $[0, 255]$ to $[-1, 1]$. We adopt the ADAM [10] optimizer with $(\beta_1, \beta_2) = (0.9, 0.999)$ and $\epsilon = 10^{-8}$ for all learnable parameters. It takes about 15 hours to learn the proposed downsampler with a single RTX 2080 Ti GPU on the synthetic DIV2K dataset. The learning time reduces to about 4 hours on the RealSR-V3 dataset as it contains fewer HR and LR samples.

APPENDIX G
ADDITIONAL QUALITATIVE COMPARISONS

We present more qualitative SR results in Figure C, D, and E. While the IKC [4] model also reconstructs clean and sharp results for some specific synthetic cases, e.g., k_1 and k_2, our combination of the AKL + RRDB [15] generalizes well with a *fixed* hyperparameter configuration, regardless of synthetic or realistic inputs. As described in our main manuscript, more qualitative results can be found from our project page: https://cv.snu.ac.kr/research/ADL.

REFERENCES

[1] E. Agustsson and R. Timofte. NTIRE 2017 challenge on single image super-resolution: Dataset and study. In *CVPR Workshops*, 2017. 5

[2] S. Bell-Kligler, A. Shocher, and M. Irani. Blind super-resolution kernel estimation using an internal-gan. In *NeurIPS*, 2019. 2, 3, 5, 6, 7

[3] J. Cai, H. Zeng, H. Yong, Z. Cao, and L. Zhang. Toward real-world single image super-resolution: A new benchmark and a new model. In *ICCV*, 2019. 6

[4] J. Gu, H. Lu, W. Zuo, and C. Dong. Blind super-resolution with iterative kernel correction. In *CVPR*, 2019. 3, 5, 6, 7

[5] M. Haris, G. Shakhnarovich, and N. Ukita. Deep back-projection networks for super-resolution. In *CVPR*, 2018. 3

[6] K. He, X. Zhang, S. Ren, and J. Sun. Deep residual learning for image recognition. In *CVPR*, 2016. 3

[7] A. Ignatov, N. Kobyshev, R. Timofte, K. Vanhoey, and L. Van Gool. DSLR-quality photos on mobile devices with deep convolutional networks. In *ICCV*, 2017. 7

[8] P. Isola, J.-Y. Zhu, T. Zhou, and A. A. Efros. Image-to-Image translation with conditional adversarial networks. In *CVPR*, 2017. 3

[9] J. Kim, J. K. Lee, and K. M. Lee. Accurate image super-resolution using very deep convolutional networks. In *CVPR*, 2016. 3

[10] D. P. Kingma and J. Ba. Adam: A method for stochastic optimization. *arXiv*, 2014. 3

[11] B. Lim, S. Son, H. Kim, S. Nah, and K. M. Lee. Enhanced deep residual networks for single image super-resolution. In *CVPR Workshops*, 2017. 3

[12] A. Radford, L. Metz, and S. Chintala. Unsupervised representation learning with deep convolutional generative adversarial networks. *arXiv*, 2015. 2

[13] A. Shocher, N. Cohen, and M. Irani. "Zero-Shot" super-resolution using deep internal learning. In *CVPR*, 2018. 5, 6, 7

[14] D. Ulyanov, A. Vedaldi, and V. Lempitsky. Instance normalization: The missing ingredient for fast stylization. *arXiv*, 2016. 2, 3

[15] X. Wang, K. Yu, S. Wu, J. Gu, Y. Liu, C. Dong, Y. Qiao, and C. Change Loy. ESRGAN: enhanced super-resolution generative adversarial networks. In *ECCV Workshops*, 2018. 3, 5, 6, 7

[16] Y. Zhang, K. Li, K. Li, L. Wang, B. Zhong, and Y. Fu. Image super-resolution using very deep residual channel attention networks. In *ECCV*, 2018. 3

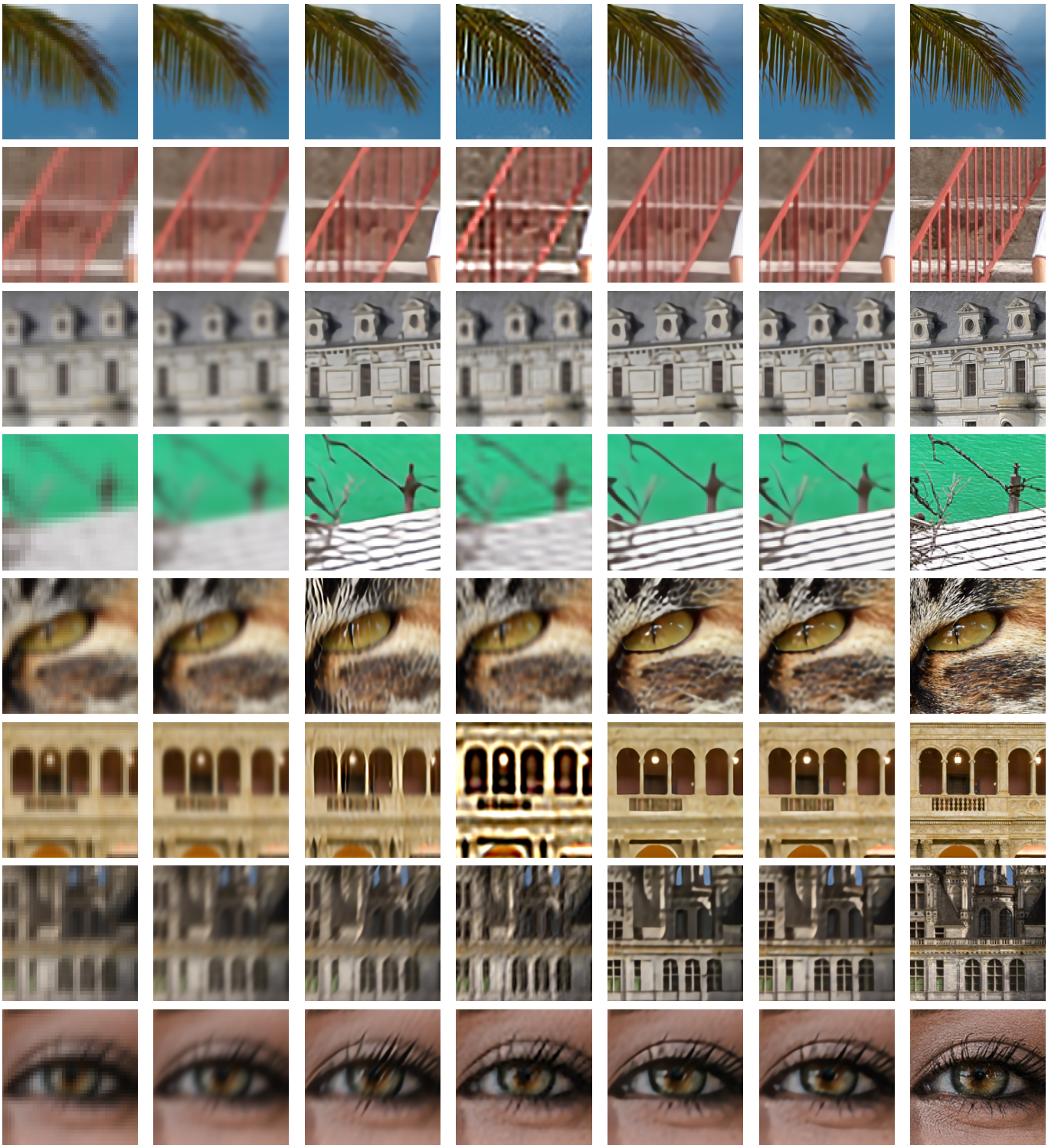

(a) $\mathbf{I}_{\mathrm{LR}}$ (Input) (b) RRDB [15] (c) IKC [4] (d) [2] + [13] (e) **ADL** + [15] (f) Oracle (g) $\mathbf{I}_{\mathrm{HR}}$ (GT)

Fig. C. **Additional qualitative $\times 4$ SR results on the synthetic DIV2K [1] dataset.** From the top, patches are cropped from the DIV2K '*0806.png* (k_1),' '*0825.png* (k_1),' '*0865.png* (k_2),' '*0807.png* (k_2),' '*0869.png* (k_3),' '*0884.png* (k_3),' '*0830.png* (k_4),' and '*0855.png* (k_4),' respectively, where LR images are synthesized using corresponding downsampling kernels in the parenthesis $(\cdot)$.

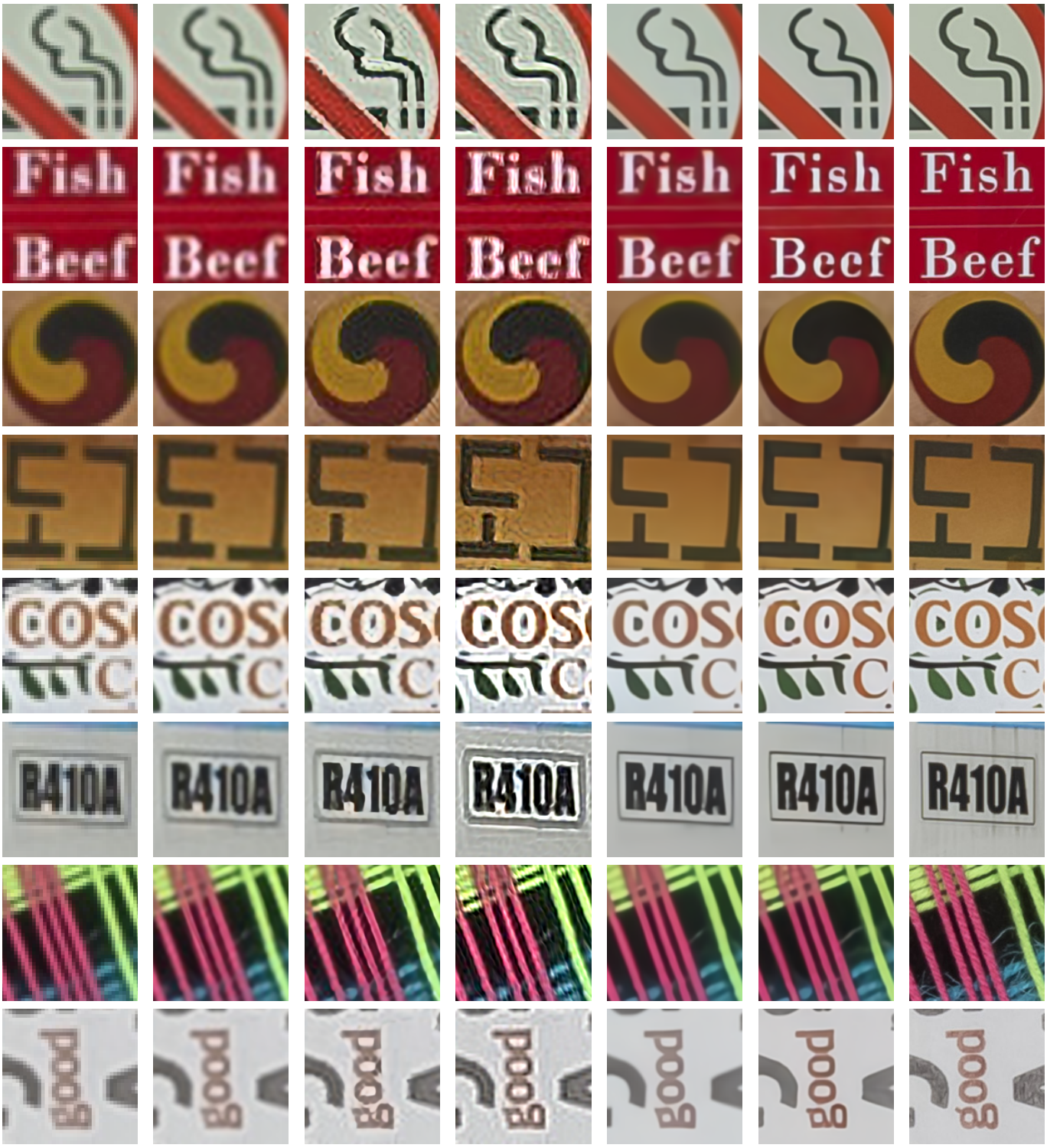

(a) $\mathbf{I}_{\mathrm{LR}}$ (Input) (b) RRDB [15] (c) IKC [4] (d) [2] + [13] (e) **ADL** + [15] (f) Oracle (g) $\mathbf{I}_{\mathrm{HR}}$ (GT)

Fig. D. **Additional qualitative $\times 4$ SR results on the RealSR-V3 [3] dataset.** From the top, patches are cropped from '*Canon/001.png*,' '*Canon/003.png*,' '*Canon/022.png*,' '*Canon/033.png*,' '*Nikon/004.png*,' '*Nikon/041.png*,' '*Nikon/049.png*,' and '*Nikon/050.png*,' respectively. Our approach (ADL + RRDB [15]) produces the least upsampling noise and artifacts in output images.

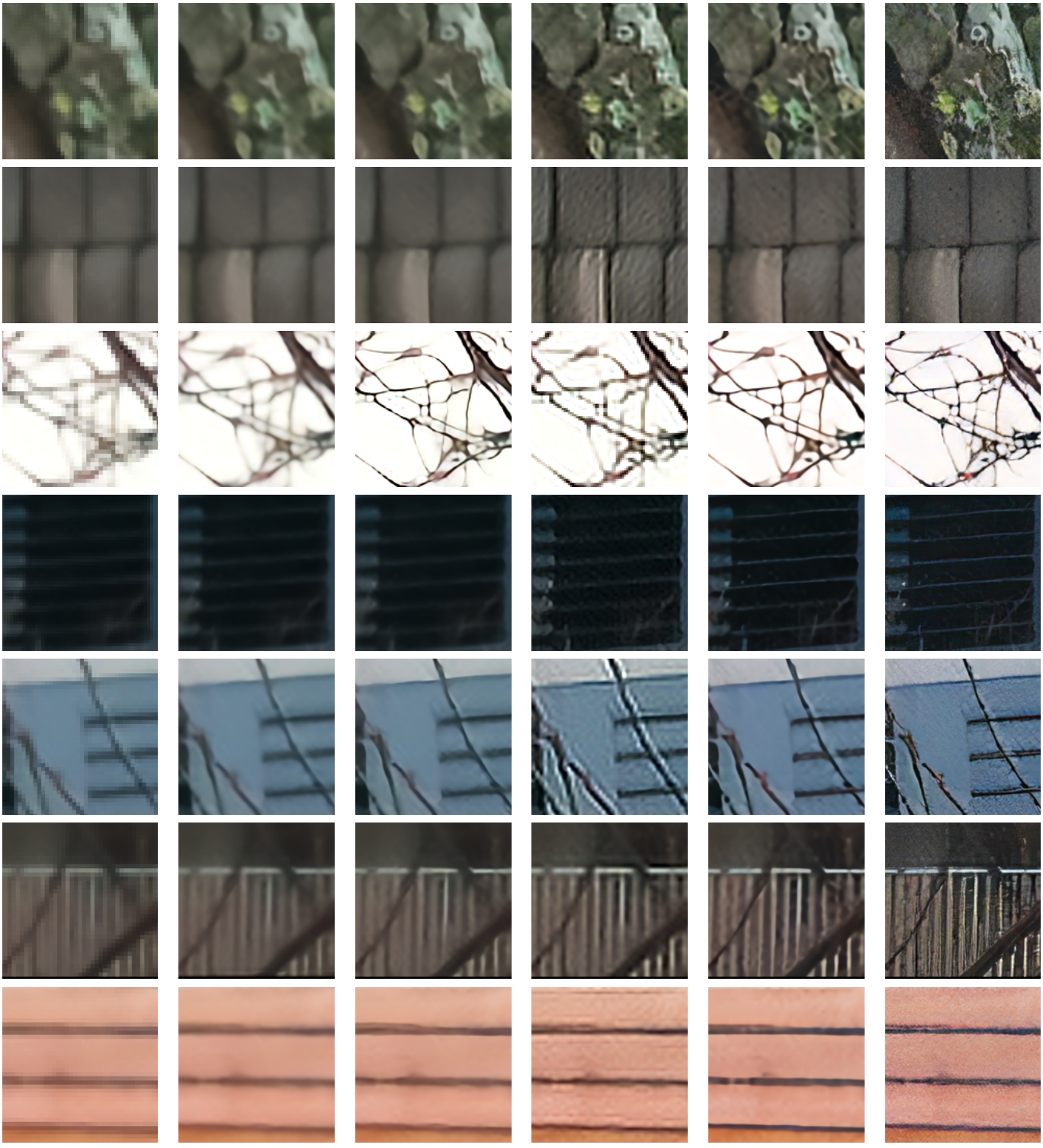

(a) $\mathbf{I}_{\text{LR}}$ (Input) (b) RRDB [15] (c) IKC [4] (d) [2] + [13] (e) **ADL** + RRDB [15] (f) **ADL** +$\mathcal{P}$

Fig. E. **Additional Qualitative $\times 4$ SR results on the DPED [7] dataset.** From the top, patches are cropped from the '*DPED-val*' '*14.png*,' '*36.png*,' '*45.png*,' '*58.png* (1),' '*58.png* (2),' '*84.png*,' and '*96.png*' respectively. We note that $\mathcal{P}$ refers to the perceptual RRDB model trained with (9) in our main manuscript. Compared to the other methods, our approaches (ADL + RRDB and ADL + $\mathcal{P}$) reconstruct sharper edges and detailed structures from given real-world LR images.